Available online at www.sciencedirect.com
SCIENCE DIRECT®
Journal of Solid State Chemistry 177 (2004) 1873–1885
JOURNAL OF SOLID STATE CHEMISTRY
http://elsevier.com/locate/jssc

Porosity, structural and fractal study of sol–gel TiO_2–CeO_2 mixed oxides

Tessy López,[a] Fernando Rojas,[a,*] Roberto Alexander-Katz,[a] Félix Galindo,[a] Alexander Balankin,[b] and Antonio Buljan[c]

[a] *Departmento de Quimica, Universidad Autónoma Metropolitana-Iztapalapa, San Rafael Atlixco 186, A. P. 55-534, México City, D.F. 09340, Mexico*
[b] *SEPI-ESIME, Instituto Politécnico Nacional, México, D.F. 07738, Mexico*
[c] *Facultad de Ciencias Químicas, Universidad de Concepción, Barrio Universitario, Casilla 160-C, Concepción, Chile*

Received 18 October 2003; received in revised form 1 January 2004; accepted 14 January 2004

Abstract

Sol–gel TiO_2–CeO_2 materials were synthesized at pH = 3 employing HNO_3 as hydrolysis agent. Gels were thermally treated at 473, 673, 873, and 1073 K, respectively. Morphologies of the final substrates were studied via N_2 sorption, XRD and TEM. N_2 isotherms indicated a steady porosity in TiO_2–CeO_2 samples treated up to 873 K. Adsorption–desorption isotherms and TEM micrographs were used to perform fractal analyses of annealed samples. A dominant anatase phase was detected by XRD between 473 and 873 K while a rutile phase was evident at 1073 K. The presence of cerium conferred an increased thermal stability to the TiO_2 materials against particle sintering and pore collapse. The structure of cerium-doped anatase lattice was visualized through crystal simulation to investigate the possible substitution of Ti^{4+} by Ce^{+4} ions. This effect and the progressive segregation of CeO_2 crystals with temperature on the surface of TiO_2 grains lead to substrates of assorted morphologies.

Keywords: TiO_2–CeO_2 materials; Cerium dispersion in titania; CeO_2 surface segregation; CeO_2-inhibited TiO_2 sintering; Xerogel fractal analysis; Xerogel pore-size distribution

1. Introduction

During the last few years TiO_2 has attracted strong attention due to its outstanding mechanical, thermal, electrical and photocatalytic properties [1]. Nevertheless, as long as a TiO_2 material can preserve: (i) a stoichiometric Ti:O molar proportion, (ii) a Ti^{4+} oxidation state, and (iii) a coordination number equal to six, then this substance behaves as an inert oxide; it is for this reason we observe the importance of creating new active titania materials by breaking up the precise TiO_2 stoichiometric formulation through doping or combination of this substance with some other compounds [2–5]. Among the lanthanide elements, cerium is the only one that forms stable compounds in a tetravalent oxidation state (i.e., Ce^{4+}) and the coordination number of surface Ce^{4+} can vary between four and eight [6,7], six and eight being the coordination numbers of bulk Ce^{4+} [8]. Furthermore, Ce ions can behave as a large O_2 trap; due to its low redox potential a Ce ion can easily pass from Ce^{4+} to Ce^{3+} [9]. Through the sol–gel procedure, it is possible to synthesize special TiO_2–CeO_2 mixed oxides by: (i) promoting the segregation and sintering of disperse CeO_2 crystallites on the surface of TiO_2 granules after thermal treatment, and/or (ii) inserting small proportions of Ce^{4+} ions within an irregular or crystalline TiO_2 network or vice versa (i.e., incorporating titanium in the ceria lattice [10]). Therefore the sol–gel technique can render feasible the creation of diluted solid titania-Ce or ceria-Ti solutions under mild conditions of synthesis in a manner similar to that by which some titanium mixed oxide systems [11,12] have been prepared. It is expected that a rather low proportion (i.e., ppm) of Ti^{4+} in the TiO_2 lattice is being substituted by Ce^{4+} due to the disparity in the ionic radii of these two species [8] (80 versus 61 pm for Ce^{4+} and Ti^{4+}, respectively, and both having a coordination number equal to six).

The performance of TiO_2–CeO_2 as outstanding ceramics, powders or thin films [1] mainly depends on the topography of the substrate surface and on the

*Corresponding author. Fax: +52-55-5804-4666.
E-mail address: fernando@xanum.uam.mx (F. Rojas).

0022-4596/$ - see front matter © 2004 Elsevier Inc. All rights reserved.
doi:10.1016/j.jssc.2004.01.013

Nomenclature

ABC	adsorption boundary curve
a_c	mean radius of curvature of the adsorbate–vapor interface
BJH	Barrett–Joyner–Halenda pore-size distribution determination method
D	pore diameter
D_B	box-counting fractal dimension method
DBC	desorption boundary curve
D_P	perimeter–area fractal dimension method
D_S	surface fractal dimension
$h\,k\,l$	crystallographic lattice planes
HL	hysteresis loop
n	amount of vapor adsorbed at a given p/p^0
NLDFT	non-local density functional theory
n_{max}	amount of vapor adsorbed at saturation
$N_{exp}(p/p^0)$	experimental isotherm data as function of the relative vapor pressure
$N_S(D,p/p^0)$	individual theoretical isotherms in pores of diameter D
$N(\Delta)$	number of boxes of linear size Δ employed in the box counting method
P	perimeter of a particle cluster with a fractal boundary
p/p^0	relative vapor pressure
PSDF	pore-size distribution function
R	universal gas constant
r	gauge of size r
S	area of a cluster with a fractal boundary
$S(r)$	surface area measured by a gauge of size r
S^{lg}	adsorbate–vapor interfacial area
T	absolute temperature
TEM	transmission electron microscope
V_m	adsorbate molar volume
XRD	X-ray diffraction
γ	liquid–vapor interfacial surface tension
$\varphi_S(D)$	NLDFT-PSDF
θ	XRD angle

porous structure of the material. In this respect, the variety of fractal dimensions of a xerogel material can provide information about the structural details of the surface, the void space and the kind of particle agglomeration array displayed by the substrate. In this work, a fractal dimension analysis of TiO_2-CeO_2 materials has been carried out by two different procedures: the Neimark-Kiselev [13] thermodynamic sorption approach and the optical analysis of transmission electron microscopy (TEM) [14–15] photographs by means of BENOIT's software (to be referenced later). In general, it can be stated that during a sol–gel transition: the aggregated solid particle conglomerates, accompanying void space, and substrate surface can all adopt fractal structures [16]. Following this point of view, the physicochemical behavior of TiO_2-CeO_2 powdery materials directly depends on the surface topography and on the morphology of the porous structure. For an irregular surface the fractal dimension D_S acquires values between two and three, so that this D_S magnitude should be found for TiO_2–CeO_2 sol–gel materials. On the other hand, the fractal dimensions D_B of the solid clusters and pore space should attain values between 1.8 and 2.1, depending on whether the aggregation process is diffusion controlled or is dominated by reactive (kinetic) factors. Additionally, the perimeter–area fractal dimension D_P should adopt values in between 1 and 2.

With respect to the pore structure parameters of the series of TiO_2–CeO_2 substrates that can be inferred from sorption processes, the pore-size distribution function (PSDF) is one of the most important features that can help in describing this type of globular porous materials. It is usual to observe that the classical BJH pore size determination [17] leads to a discrepancy [18] between the results obtained from the analyses of the adsorption boundary curve (ABC) and the desorption boundary curve (DBC) that set the limits of the hysteresis loop (HL) of the sorption isotherm. This is due to two main reasons: (i) the neglect of attractive or repulsive forces between molecules during capillary condensation and capillary evaporation (this disregard leads to misleading inferences about the geometry of the meniscus and its stability during capillary condensation/evaporation and consequently to deceptive pore sizes); (ii) the presence of pore-networking or pore-blocking effects. By reason of the preceding arguments, in this work we have preferred the non-local density functional theory (NLDFT) approach to evaluate the PSDF since this method eliminates some of the most important shortcomings inherent to the BJH analysis [19,20], mainly because it takes into account the variety of interaction potentials (i.e., solid–adsorbate, adsorbate–adsorbate, etc.) existing in the adsorption system and also because it can shed light about some of the particularities of the mechanistic aspects of the evaporation and condensation processes that are taking place inside the cavities and throats [21] that constitute the void space of the gel arrangement. This latter statement arises after observing the results of the NLDFT method to determine pore sizes in model cylindrical MCM-41 and SBA-15 porous solids [22,23]. It is now accepted [24] that a classical BJH analysis, if compared to either NLDFT or electron microscopy determinations, renders pore sizes smaller than the real

ones by as much as several nanometers, mainly due to the disregard of the adsorption potential emerging from the pore walls that is inherent to the classical BJH method. The existence of an adsorption potential within the pores of a substrate causes an enhanced stability of incumbent fluid phases against the capillary (i.e., surface tension) driving forces that would lead to the successive coalescence and movement of liquid–vapor menisci. Nevertheless, both BJH and NLDFT methods require explicit pore geometries. In general, the ink-bottle structure of sol–gel materials is closely associated to the globular model of porous substrates [25] and therefore in the present work we adopt the ink-bottle geometry as our departing pore model that will be finally simplified to a cylindrical geometry after analyzing the PSDF outcome.

2. Principal methods and techniques employed to characterize sol–gel TiO_2–CeO_2 materials

2.1. PSDFs determined from N_2 sorption

The NLDFT approach [26,27] calculates the theoretical adsorption–desorption isotherms in pores of given shapes. Moreover, the experimental isotherm of porous materials constituted, for instance, of cylindrical capillaries or slit-shaped pores of different sizes, can be approximated by a convolution of the theoretical NLDFT isotherms as

$$N_{\exp}(p/p^0) = \int_{D_{\min}}^{D_{\max}} N_S(D, p/p^0)\varphi_S(D)\,\mathrm{d}D. \quad (1)$$

Here, $N_{\exp}(p/p^0)$ represents the experimental isotherm (i.e., the amount adsorbed at each relative vapor pressure p/p^0 value), $N_S(D, p/p^0)$ corresponds to individual theoretical NLDFT isotherms in pores of diameter D, and $\varphi_S(D)$ is the PSDF to be determined. The optimal numerical inversion of Eq. (1) provides the best $\varphi_S(D)$ fit to the $N_{\exp}(p/p^0)$ set of experimental data; NLDFT calculation software is now available to perform PSDF determinations from isotherm data in model (e.g., cylindrical, slit-like or ink-bottle) systems.

2.2. Neimark–Kiselev (NK) method for the determination of the surface fractal dimension

Porous materials are characterized by a surface fractal dimension D_S defined as

$$S(r) \approx (r)^{2-D_S}, \quad (2)$$

where $S(r)$ is the surface area measured by a gauge of size r. Neimark [13] proposed a thermodynamic sorption approach to determine D_S where r corresponds to the mean radius of curvature of the adsorbate vapor interface a_c given by the Kelvin equation:

$$a_c = \frac{2\gamma V_m}{RT\ln(p^0/p)} \quad (3)$$

$S(r)$ is expressed in terms of the adsorbate–vapor interfacial area S^{lg} that, in turn, is given by the Kiselev equation [28]:

$$S^{lg} = \frac{RT}{\gamma}\int_n^{n_{\max}} \ln\left(\frac{p^0}{p}\right)\mathrm{d}n. \quad (4)$$

With R being the universal gas constant; T the adsorption temperature; γ the $l-g$ interfacial surface tension; V_m the adsorbate molar volume; p/p^0 the relative pressure (where p^0 is the saturation pressure); and finally, n and $n_{\max}$ are the amounts of gas adsorbed at p/p^0 and at saturation, respectively.

2.3. Other fractal dimensions

The box fractal dimension D_B is defined as the exponent in the relationship

$$N(\Delta) \propto \Delta^{-D_B}, \quad (5)$$

where $N(\Delta)$ is the number of boxes of linear size Δ necessary to cover a data set of points distributed on a two-dimensional plane. The perimeter–area fractal dimension D_P is defined by the relation

$$S^{D_P} \propto P^2 \quad (6)$$

between area S and perimeter P of a particle cluster with a fractal boundary [29].

Both perimeter and area fractal dimensions of our TiO_2–CeO_2 substrates were measured by the box-counting method.

3. Experimental

3.1. Materials and synthesis

TiO_2–CeO_2 materials (90 wt% TiO_2–10 wt% CeO_2, respectively) were prepared by the sol–gel method using titanium *n*-butoxide (Aldrich 97 wt%) and cerium nitrate (Aldrich 99.9 wt%) as essential reactants. Ethanol (99 wt%) was chosen as the solvent medium of the latter substances and a molar alkoxide/solvent ratio of 1/16 was selected. The mixture was kept refluxing while adjusting to pH = 3 with HNO_3 during the entire sol synthesis; the pH being continuously monitored by means of a potentiometer. Afterwards, water, in a molar proportion of 1:8 with respect to the Ti alkoxide, was added dropwise during a period of 4 h. The above reactant quantities and the slow H_2O addition mode were chosen with the aim of attaining a significant interaction between all incumbent ions and suitable hydrolyzed species (i.e., –Ti–OH; –Ti–O^-; –Ti–OBut).

The reactant mixture was kept refluxing until a gel was formed; a xerogel ensued after the latter colloid was air-dried at 343 K for 24 h. Four powdery substrates were obtained from the thermal treatment of precursor xerogels in air at 473, 673, 873, and 1073 K, respectively. The selected final temperature was attained after undergoing a heating ramp of 2 K min^{-1}; each solid specimen was kept at its respective ultimate temperature condition for further 4 h. The samples obtained were labelled in the following way: TiO_2–CeO_2-(annealing Kelvin temperature), e.g., TiO_2–CeO_2-473, TiO_2–CeO_2-673, etc. Additionally, blank (i.e., cerium-free) TiO_2 samples were also synthesized under the same synthesis conditions and calcination temperatures in order to employ these solids as reference materials; labelling of TiO_2 samples was similar to that described above, i.e., TiO_2-473, TiO_2-673, etc.

3.2. Characterization

3.2.1. Adsorption measurements

N_2 sorption isotherms at 76 K (this is the boiling temperature of N_2 at Mexico City, i.e., 2200 m above sea level) on TiO_2–CeO_2 substrates were determined by means of an automatic Quantachrome Autosorb 3B instrument. Prior to the adsorption run, all samples were outgassed overnight at 473 K. N_2 and He gases required for the operation of the sorption apparatus were UHP grade.

3.2.2. Electron microscopy

TiO_2–CeO_2 samples were embedded in an epoxy resin (Epon 12), and dried at 333 K for 24 h in order to cure and aging the resin. 80 nm thin sections were cut by means of an RMC-MT7000 microtome operating at cryogenic conditions (153 K) and afterwards deposited on a copper grid and carbon coated inside a Blazers evaporator. Finally the samples were observed by TEM with a Leo EM-910 (120 kV) electron microscope.

3.2.3. Fractal dimension

For the determination of fractal dimensions, TiO_2–CeO_2 TEM micrographs were analyzed and transformed into a histogram of a gray-scale image. The gray-scale image was black–white converted using the histogram maximum as threshold value. The fractal dimensions of solid clusters D_B was determined by the box-counting method [14,29] using the commercial BENOIT 1.2 software [30]. The fractal dimension D_P of cluster boundaries (cluster–pore interface) was determined through the perimeter–area method, also included in the BENOIT software.

3.2.4. XRD

Diffraction powder patterns were recorded via a Siemens D-500 diffractometer system employing a Cu$K\alpha$ radiation using a 0.02° step size and a measuring frequency of 2.4 s^{-1} in the scattering (2θ) range between 20° and 110°. The lattice reflections (*hkl*) that have been considered to simulate the experimental spectra through the Rietveld refinement procedure correspond to those listed in the Joint Committee on Powder Diffraction Standards (JCPDS) cards, i.e., anatase, rutile and ceria JCPDS cards No. 83-2243, 75-1752 and 34-0394, respectively). The anatase phase displays prominent XRD peaks originated from (101) planes at a diffraction angle of $2\theta = 25.2°$, from (004) planes at $2\theta = 37.8°$ and from (200) planes at $2\theta = 48.1°$ (i.e., the first three peaks that can be seen in the refined spectra of Figs. 3a–c). In turn, the main (*hkl*) reflections considered for rutile were those proceeding from the (1, 1, 0), (1, 0, 1), (1, 1, 1), and (2, 1, 1) planes, i.e., $2\theta = 27.4°$, 36.1°, 41.2°, and 54.3°. Some of the main reflections which are characteristic of CeO_2 cubic phase correspond to the crystal planes (111), (002) and (220), i.e., to diffraction angles of 28.6°, 33.1° and 47.5°, respectively.

4. Results and discussion

4.1. Adsorption results

4.1.1. General characteristics

N_2 isotherms of samples TiO_2–CeO_2-473, TiO_2–CeO_2-673, and TiO_2–CeO_2-873 (Fig. 1) display type H2 hysteresis loops [31], a characteristic proper of many sol–gel materials; while specimen TiO_2–CeO_2-1073 portrays practically no hysteresis and almost matches

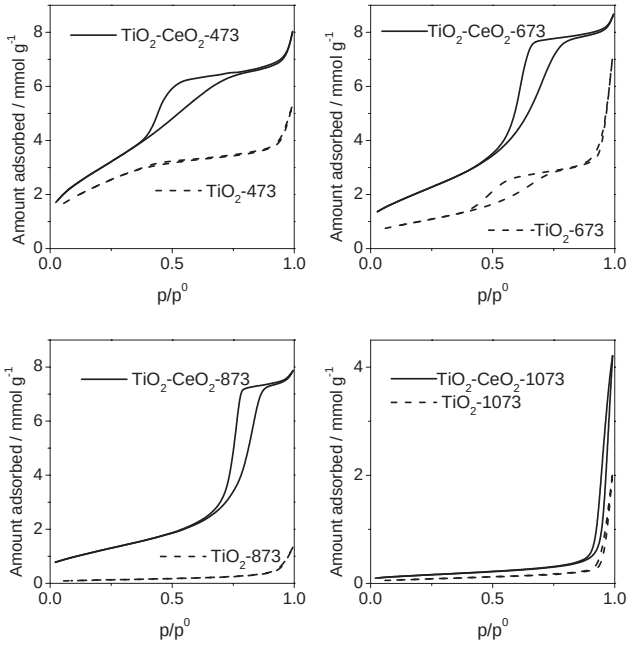

Fig. 1. N_2 sorption isotherms at 76 K on TiO_2–CeO_2 and TiO_2 substrates annealed at different temperatures.

a Type 2 isotherm [32], a quality that is usually credited to a non-porous adsorbent. For comparison purposes, the sorption isotherms due to cerium-free TiO_2 systems are also included in Fig. 1. From these curves it was possible to evaluate the surface areas and the pore volumes of all TiO_2–CeO_2 and TiO_2 samples (Table 1).

The first thing to note about the N_2 sorption isotherms of hybrid TiO_2–CeO_2 samples is the enhanced thermal stability of their porous structures if compared to those of Ce-free TiO_2 substrates. Both the surface area and pore volume values of TiO_2–CeO_2 substrates are significantly larger than those related to the TiO_2 materials. While the TiO_2–CeO_2-873 sample is still depicting appreciable pore volume and surface area as well as a manifest hysteresis loop, the TiO_2-873 is practically a fused mass having no pores. A characteristic inherent to both hybrid and non-hybrid specimens treated at 1073 K is that N_2 sorption curves are Type 2 isotherms, i.e., curves suitable to non-porous solids. Therefore, it seems that the degree of sintering of TiO_2 globules in hybrid materials is appreciably diminished by the presence of cerium in the range of temperatures extending from 473 to 873 K; in order to explain this fact, we will advance two hypotheses that will be justified after discussing XRD results and trying to visualize a Ce-doped anatase structure: (i) the emergence of CeO_2 crystals onto the surface of TiO_2 particles can keep two titania globules sufficiently away, thus preventing them from joining together at temperatures at which a pure titania lattice normally sinters; (ii) additionally, substitution of Ti^{4+} ions by Ce^{4+} ions in the TiO_2 lattice may further stabilize the structure against the sintering process.

The H2 character of the TiO_2–CeO_2 materials prepared at temperatures between 473 and 873 K suggests that the void structure is made by the interconnection of ink-bottle pores, i.e., void arrangements consisting of void chambers interconnected by narrower necks. As a consequence of their H2 character; isotherms corresponding to TiO_2–CeO_2-473, TiO_2–CeO_2-673, and TiO_2–CeO_2-873 samples depict an additional noteworthy characteristic: the existence of a plateau that extends from high to intermediate relative vapor pressures along the DBC of the isotherms, thus indicating the incidence of a well-defined total pore volume in these substrates. Also, in conjunction with the H2 character, TiO_2–CeO_2 samples treated at temperatures between 473 and 873 K are entirely mesoporous solids (this fact was later confirmed by a *t*-plot analysis [32] performed on each sample). Additionally, a very slight macropore contribution can be accounted for the asymptotic behavior of the isotherms of the latter samples at around $p/p^0 \sim 1$.

For simplicity, in this work we shall represent the complex ink-bottle structure by a collection of cylindrical pores. The validity of this simplification will be discussed later in this work, although one important reason for this assumption would be that the sizes of cavities and their surrounding pore necks are not too different from each other, especially for samples annealed at higher temperatures. Under this simplified pore geometry, capillary condensation of vapor in the voids conforming a globular aggregate takes place when the adsorbed film on a given pore throat attains a critical thickness. The liquid filling of the throats that surround a given pore cavity can then lead to the formation of liquid–vapor menisci that can either advance straightforwardly into the chamber or remain anchored at the pore entrance until the vapor pressure attains a sufficiently high value for the chamber to be overtaken by condensate [21].

The PSDF of TiO_2–CeO_2 materials has been calculated by the NLDFT procedure applied to both ABC and DBC branches of the sorption isotherm [22,23]. Although the NLDFT approach was initially designed to be used in conjunction with sorption equilibrium data arising from the DBC, the comparison between NLDFT-ABC and NLDFT-DBC will shed light upon

Table 1
Surface areas and pore volumes of TiO_2 and TiO_2–CeO_2 samples

Substrate	Surface area/$m^2\,g^{-1}$			Pore volume/$mm^3\,g^{-1}$		
	A_{BET}	$A_{DBC\text{-}NLDFT}$	$A_{ABC\text{-}NLDFT}$	$V_{NLDFT\text{-}DBC}$	$V_{NLDFT\text{-}ABC}$	$V_{p/p0=0.95}$
TiO_2-473	195	139	140	152	168	136
TiO_2-673	83	69	72	107	102	111
TiO_2-873	10	8.1	8.4	31	39	18
TiO_2-1073	7	5	5	10	10	11
TiO_2–CeO_2-473	252	190	187	242	257	241
TiO_2–CeO_2-673	176	159	160	276	281	279
TiO_2–CeO_2-873	100	99	105	257	257	258
TiO_2–CeO_2-1073	12	12	14	113	122	32

A_{BET}: BET surface area; $A_{DBC\text{-}NLDFT}$: NLDFT surface area; determined from the desorption boundary curve (DBC); $A_{ABC\text{-}NLDFT}$: NLDFT surface area; determined from the adsorption boundary curve (ABC); $V_{NLDFT\text{-}DBC}$: cumulative NLDFT-DBC pore volume; $V_{NLDFT\text{-}ABC}$: cumulative NLDFT-ABC pore volume; $V_{p/p0=0.95} \equiv$pore volume determined from the ABC at a relative vapor pressure $p/p^0 = 0.95$.

irreversible phenomena occurring during desorption, since the ABC isotherm is supposed to be relatively free of irreversible processes [33]. Also some key morphological aspects of the porous structure of TiO_2–CeO_2 materials will be evident after performing this comparison.

It may happen very often that, in the case of disordered globular arrays [34], some of the pore necks are not very different in size if compared to the diameter of the cavity that all these throats surround; this causes that the condensate uptake of the pore openings around a cavity occurs almost concurrently with the chamber invasion by liquid. This filling feature [35] is mainly due to the limited polydisperse character shown by the globules forming a gel arrangement; in this case it has been suggested that an average connectivity number of about four applies [34] (i.e., an average of four neighboring globules are delimiting a cavity). Owing to these characteristics, in many xerogel aggregates, throat sizes assume control of both adsorption and desorption processes; for easiness, the geometry of the menisci during capillary condensation can be assumed as cylindrical (in view of the tubular nature of the throats at which condensation starts), while the meniscus shape would likely be hemispherical during capillary evaporation (i.e., these adsorption–desorption mechanisms would be similar to those arising in a cylindrical pore [36]).

4.1.2. Pore-size distributions

The PSDF curves corresponding to the series of TiO_2–CeO_2 samples are shown in Fig. 2; for comparison purposes, the PSDFs of substrates TiO_2-473 and TiO_2-673 are also shown in Fig. 2 (PSDFs of samples TiO_2-873 and TiO_2-1073 have not been determined since there are practically no pores inside these materials). Table 2 shows the mean pore sizes calculated from NLDFT-ABC and NLDFT-DBC treatments.

Details are as follows: from the PSDF of specimen TiO_2–CeO_2-473, one can confirm that some vapor percolation arises at some point along the DBC; this irreversible phenomenon is evident from the isotherm and can be assessed by comparing the ABC- and DBC-NLDFT PSDF curves. The DBC-NLDFT is sharper than the ABC-NLDFT PSDF (see Fig. 2a). This means that some pore-blocking [37] of cavities having sizes larger than 5.5 nm (see area B in Fig. 2a) occurs during the development of the DBC on this sample; all these pores suffer a vapor percolation at some point of the DBC (see area A in Fig. 2a). Interestingly, although area A is close in value to area B, these regions adopt, however, different shapes, thus indicating somehow that the inkbottle pores of this sample have cavity diameters which are not excessively different from their throat widths and that the arrangement of nanometric globules in this xerogel is mostly random (i.e., one depicting a mean connectivity of about 4) while the particle size distribution consists of nearly monodisperse globules. A TEM micrograph of the TiO_2–CeO_2-473 specimen (Fig. 3b) shows the fairly loose structure of this sample. The PSDF of ceria-free TiO_2-473 specimen (see Fig. 3e) shows a different characteristic if compared to the TiO_2–CeO_2-473 outcome: the results from ABC and DBC curves practically coincide into one curve, thus meaning that the porous structure of this TiO_2 material is still wide open to both the uptake and dislodgment of condensate and meaning that sintering has not yet taken place extensively in this sample.

The DBC-NLDFT and ABC-NLDFT PSDF curves of specimen TiO_2–CeO_2-673 (Fig. 2b) achieve a finer agreement, thus reinforcing the idea of having pretty similar cavity and throat sizes in this substrate and also reflecting the fact that this pore structure is suffering a relatively slight pore-blocking phenomenon along the DBC. On the other hand, N_2 adsorption on pore entities along the ABC occurs almost freely of any delaying effects (also as a consequence of the proximity in sizes between cavities and throats). It is important to note that the average pore size (Table 2) of this specimen is larger than the value corresponding to TiO_2–CeO_2-473; this can mean that a sintering process is taking place in TiO_2–CeO_2-673 as the temperature is raised since the BET surface area is lower than for specimen TiO_2–CeO_2-473, but still the total pore volume is roughly similar for the two samples. Fig. 3c shows a TEM micrograph of this sample and in which the effects of a sintering process are evident. The PSDF of sample TiO_2-673 (Fig. 2f) shows the presence of necks and cavities, therefore the TiO_2 globules are becoming closer to each other and some sintering starts taking place (a TEM photograph of this sample can be seen in Fig. 3a). In the same way a pore-blocking effect of a certain intensity is taking place when N_2 is desorbed from the pores of this material.

With respect to the ABC-NLDFT and ABC-NLDFT PSDFs of specimen TiO_2–CeO_2-873 (see Fig. 2c), a reasonably good agreement between the two results has been attained. In general, this sample behaves similarly as TiO_2–CeO_2-673 toward N_2 sorption, although the mean pore size of TiO_2–CeO_2-873 is larger as a consequence of the progress of the sintering process with temperature. Then again, a slight pore-blocking effect is due to the special inkbottle nature of the porous structure of this substrate and in which chambers and necks are comparable in size. Fig. 3d depicts the structure of the material as observed by TEM.

The DBC-NLDFT and ABC-NLDFT PSDF curves of specimen TiO_2–CeO_2-1073 point to very large pore sizes (Fig. 2d), since this substrate constitutes a non-porous material due to the crystalline phase change (anatase → rutile) and sintering processes that experience the titania globules during their thermal treatment up to

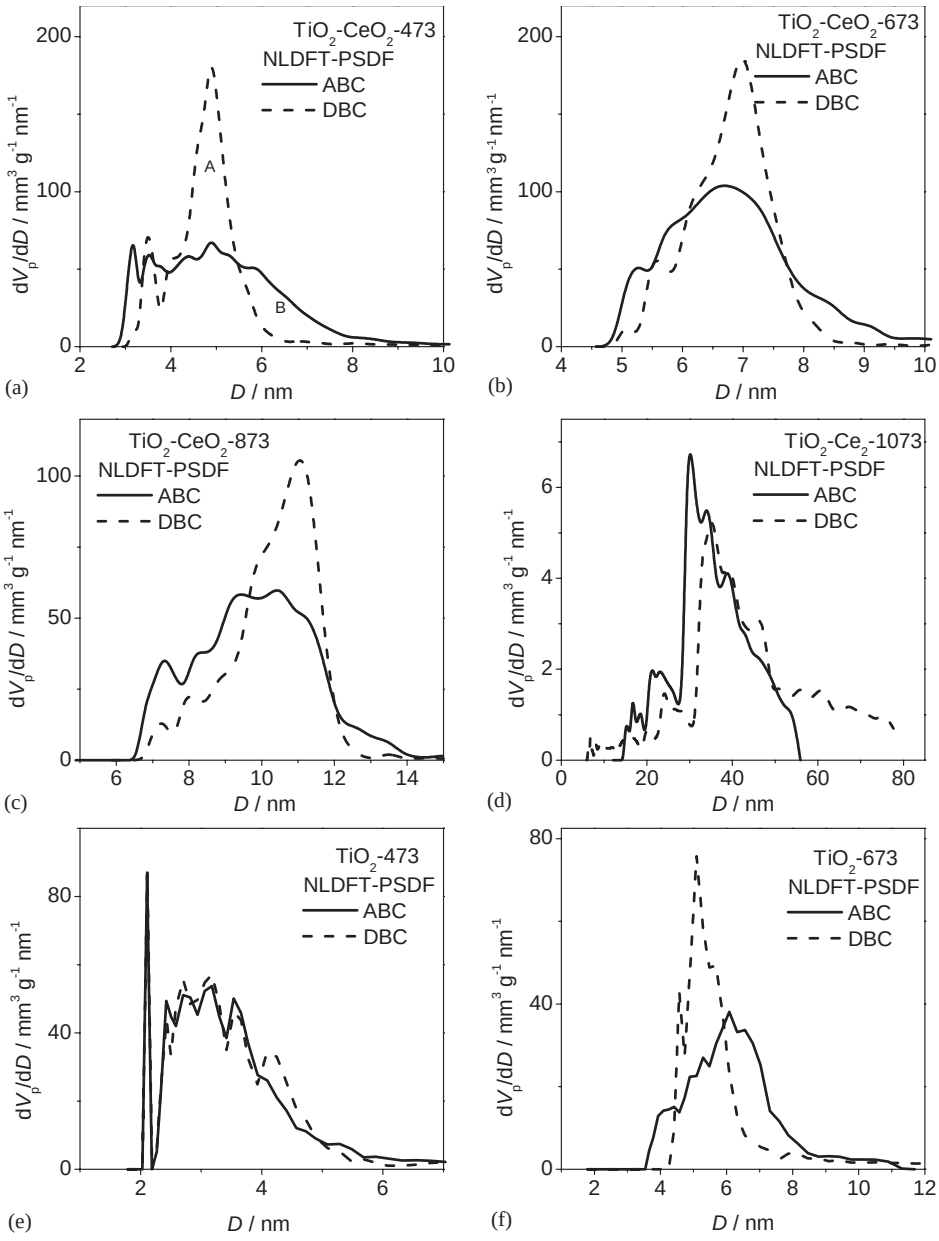

Fig. 2. NLDFT-PSDFs of TiO_2–CeO_2 materials annealed at different temperatures. (a) TiO_2–CeO_2-473, (b) TiO_2–CeO_2-673, (c) TiO_2–CeO_2-873, (d) TiO_2–CeO_2-1073, (e) TiO_2–473, and (f) TiO_2-673.

Table 2
Mean pore sizes (nm) and standard deviations (nm) of TiO_2 and TiO_2–CeO_2 substrates calculated from NLDFT measurements

Sample	$D_{NLDFT\text{-}ABC}$	$\sigma_{NLDFT\text{-}ABC}$	$D_{NLDFT\text{-}DBC}$	$\sigma_{NLDFT\text{-}DBC}$
TiO_2-473	3.2	0.7	3.2	0.8
TiO_2-673	6.0	1.1	5.3	0.5
TiO_2-873	29	28	30	27
TiO_2-1073	12	11	15	15
TiO_2–CeO_2-473	5.2	1.4	4.9	0.3
TiO_2–CeO_2-673	6.8	1.0	6.9	0.6
TiO_2–CeO_2-873	10.1	1.6	10.7	0.8
TiO_2–CeO_2-1073	37	9	40	7.0

$D_{NLDFT\text{-}ABC}$: NLDFT-ABC mean pore size; $D_{NLDFT\text{-}DBC}$: NLDFT-DBC mean pore size; $\sigma_{NLDFT\text{-}ABC}$: NLDFT-ABC pore size standard deviation; $\sigma_{NLDFT\text{-}DBC}$: NLDFT-DBC pore size standard deviation.

1073 K; additionally, this sample contains CeO_2 as a segregated cerianite phase as it is explained below.

4.2. XRD studies

Fig. 4 depicts XRD patterns of TiO_2–CeO_2 solids treated at different temperatures. These spectra have been refined by the Rietveld method [38] in order to achieve an easier visualization of the nanocrystalline phases forming part of the structure of the diverse TiO_2–CeO_2 xerogels specimens. In the Rietveld method, the powder XRD diffraction pattern calculated from a trial structure is compared with the experimental powder diffraction pattern. The calculated (top) and the

difference (bottom) powder patterns of Rietveld refined spectra can be seen in Fig. 4 (Bragg lattice reflection positions of anatase, and if applicable, those of rutile and ceria phases are marked by vertical bars below each refined spectrum). The RWP factor (i.e., the so-called weighted powder profile *R*-factor) quantifies the result of the comparison procedure; the smaller this RWP factor the better the agreement between the trial and the experimental structures. Table 3 shows the abundances of crystalline phases and the RWP factor determined for the set of TiO_2–CeO_2 samples; moreover, Table 3 also shows mean crystal sizes, unit cell parameters and densities of the crystalline phases present in TiO_2–CeO_2 materials. Crystal sizes and unit cell parameters of ceria-free titania samples (i.e., TiO_2-473, TiO_2-673, etc.) are also reported in Table 3 in order to compare these values with those of the ceria-doped samples. As a result, the following important characteristics can be drawn from the analysis of Rietveld refined XRD spectra, namely:

- The TiO_2–CeO_2 samples constitute indeed nanocrystalline arrangements embedded in an amorphous environment (i.e., the crystalline and the difference contributions of the Rietveld-refined spectrum denote the presence of these regular and amorphous media).
- Crystalline TiO_2 exists solely as anatase between 473 and 873 K from which point onwards the rutile phase starts nucleating to become the dominant one at 1073 K. It can be thought that one important effect of Ce atoms is to stabilize to some extent the anatase

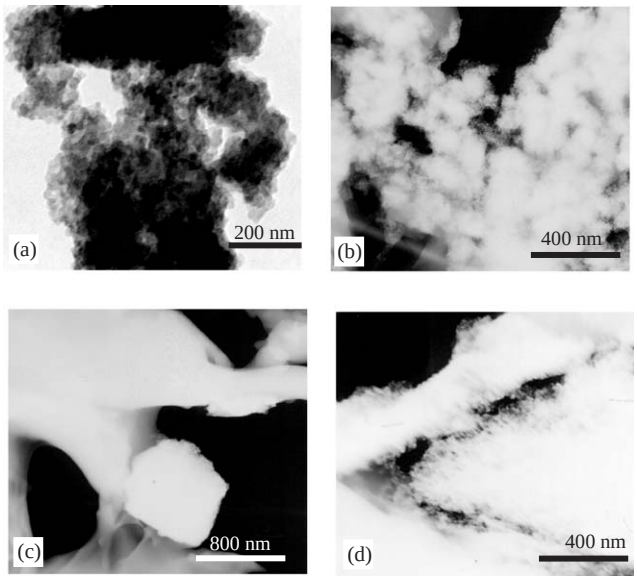

Fig. 3. TEM micrographs of: (a) TiO_2-673 (50,000 ×), (b) TiO_2–CeO_2-473 (50,000 ×), (c) TiO_2–CeO_2-673 (25,000 ×), and (d) TiO_2–CeO_2-873 (50,000 ×).

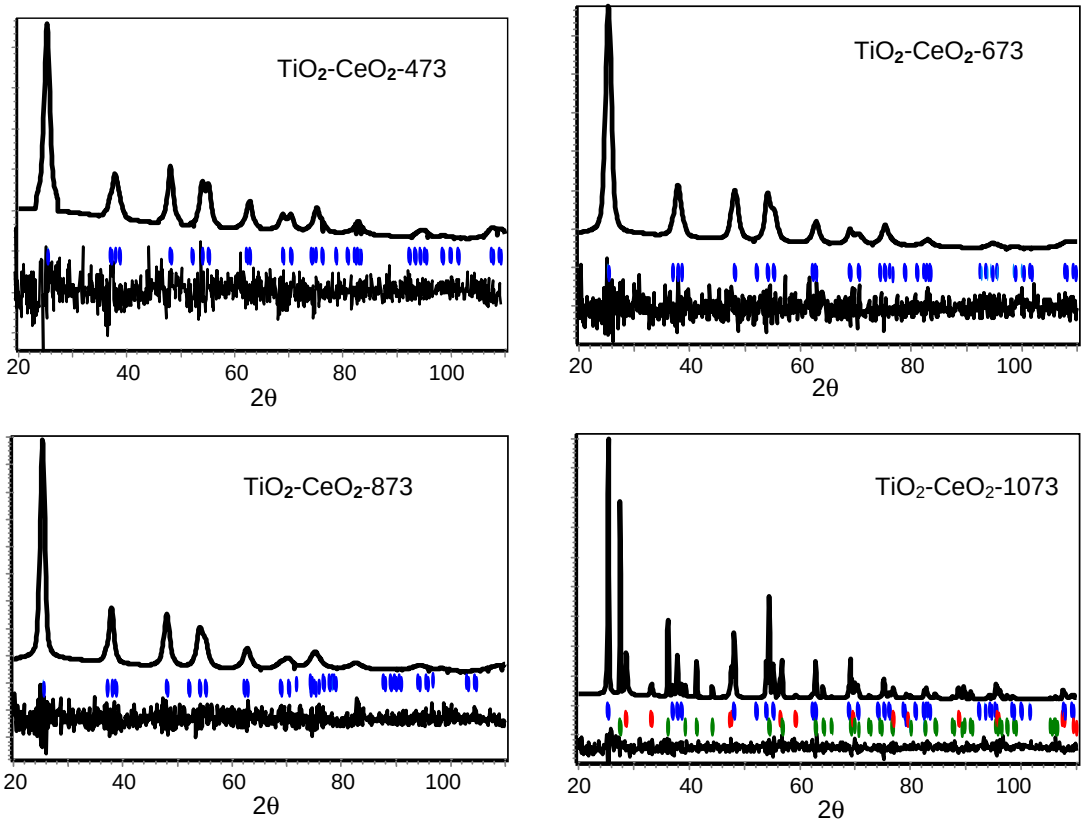

Fig. 4. Rietveld refined XRD spectra of TiO_2–CeO_2 materials. The upper curve in each figure corresponds to Rietveld refined diffraction pattern while the lower curve is the difference pattern between trial and experimental spectra. Bragg reflections are indicated by vertical bars (|) below the refined spectra according to the following position order: anatase (top), ceria (middle) and rutile (bottom).

Table 3
Abundance of crystalline phases, mean crystal sizes, unit cell parameters (a, b, c) and densities (ρ) of anatase (A), rutile (R) and cerianite (C) phases in TiO_2–CeO_2 and TiO_2 materials

	TiO_2–CeO_2-473 TiO_2-473	TiO_2–CeO_2-673 TiO_2-673	TiO_2–CeO_2-873 TiO_2-873	TiO_2–CeO_2-1073 TiO_2-1073
Anatase wt%	100 100	100 100	100 100	56.4 7.9
Rutile wt%	0 0	0 0	0 0	37.5 92.1
Cerianite wt%	0 0	0 0	0 0	6.0 0
RWP	25.5 23.5	20.3 17.7	19.5 10	15.2 10.3
Crystal size (Å)	9.4 17.6	31.4 19.5	105.3 54.4	108.9(A), 359.3(R), 20.6(C) 86.7(A), 387.6(R)
a (Å)	3.999 3.791	3.785 3.759	3.733 3.781	3.777(A), 4.582(R), 5.397(C) 3.785(A), 4.595(R)
b (Å)	3.999 3.791	3.785 3.759	3.733 3.783	3.777(A), 4.582(R), 5.397(C) 3.785(A), 4.595(R)
c (Å)	9.981 9.437	9.513 9.424	9.358 9.520	9.499(A), 2.953(R), 5.397(C) 9.516(A), 2.959(R)
ρ ($g\,cm^{-3}$)	3.327 3.912	3.892 3.984	4.066 3.894	3.913(A), 4.277(R), 7.267(C) 3.891(A), 4.245(R)

phase [39] beyond the typical temperature values ($\sim$873 K) that are usually needed to transform the pure phase into rutile [40].

- As the temperature is raised the TiO_2–CeO_2 spectra are sharper and the Ce atoms are progressively segregated from the anatase structure that, in consequence, becomes denser. The anatase unit cell exists somewhat expanded at low temperatures thus suggesting that the presence of Ce atoms distort to some extent the anatase crystalline structure; the densities of ceria-free TiO_2 samples at low temperature are rather larger than those of the ceria-doped materials.
- There is no much evidence about the presence of Ce atoms inside the rutile phase at 1073 K by reason of the sharp XRD peaks and similar densities displayed by both ceria-free and ceria-doped TiO_2 specimens.
- Cerianite crystals give distinctive signals at 1073 K; it may be possible that very small nanocrystals of this compound could already be formed at lower temperatures but due to their minute sizes clear XRD signals cannot be discerned. This can also mean that cerium atoms exist first in the form of a very disperse phase in either the amorphous or TiO_2 crystalline structures and then start growing and sintering to constitute larger and larger CeO_2 crystallites as the annealing temperature is increased.

4.3. Fractal analysis

Fig. 5 shows the results of Neimark analysis of the adsorption–desorption isotherms of TiO_2–CeO_2 materials at each sintering temperature. As one can see from Table 4, the fractal dimension D_S obtained via the adsorption branch differs very little from that obtained through the desorption isotherm. However, the fractal dimension obtained by this method is sensitive to the thermal treatment as shown in Table 4. As we increase the sintering temperature the fractal dimension decreases and the relative pressure range, where fractality holds, increases (except for the sample at 1073 K). By means of the Kelvin equation, one can induce from Fig. 5 that fractality holds for gauges of sizes smaller than 0.96 nm at 473 K, 1.57 nm at 673 K and 2.6 nm at 873 K. This implies that the fractality values obtained by adsorption–desorption methods are in a region of probes significantly smaller than the mean pore size for these systems and therefore the observed fractal dimension should describe the surface fine details within the pores. Besides, the decrement in D_S with temperature implies a smoothing of the pore walls thus

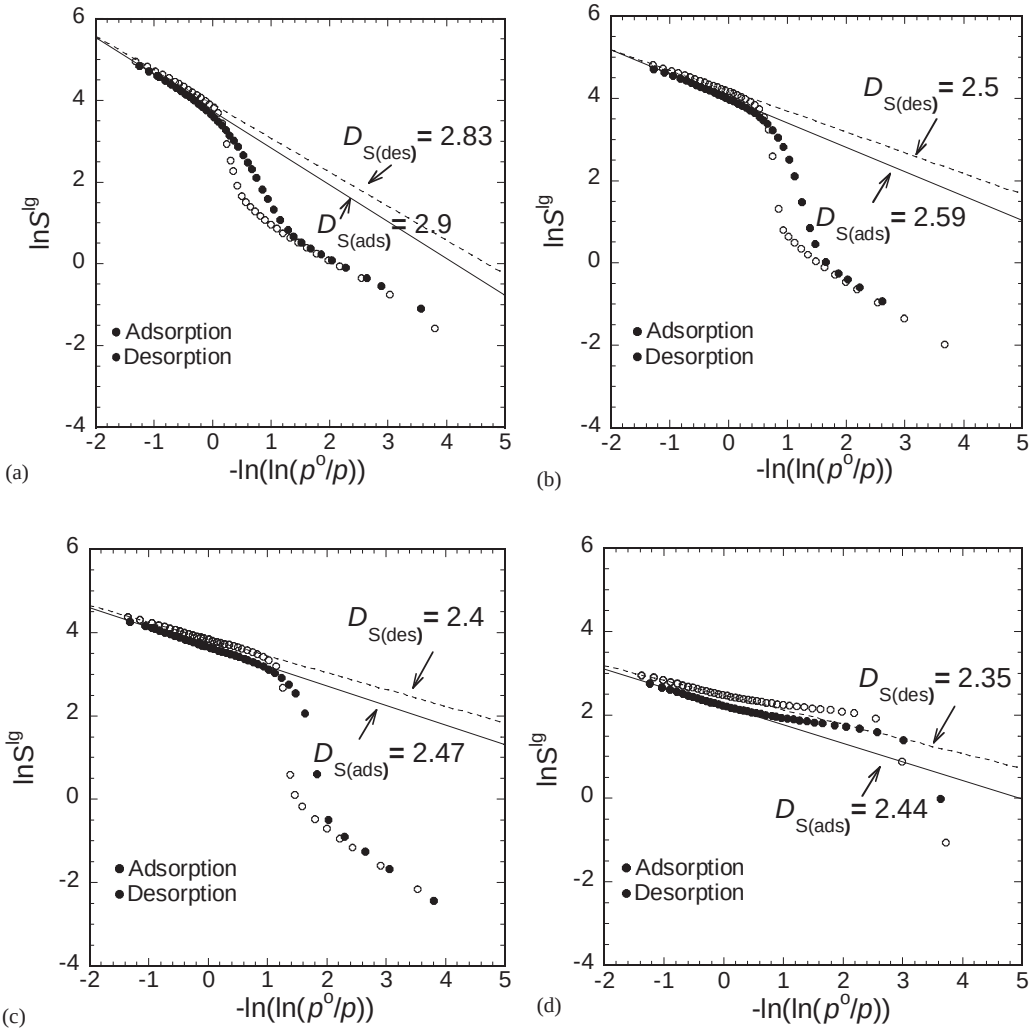

Fig. 5. Neimark fractal analysis of the adsorption–desorption isotherms of TiO_2–CeO_2 substrates. (a) 473 K, (b) 673 K, (c) 873 K, and (d) 1073 K.

Table 4
Summary of fractal dimensions of TiO_2–CeO_2 substrates

Method of analysis	TiO_2–CeO_2-473	TiO_2–CeO_2-673	TiO_2–CeO_2-873	TiO_2–CeO_2-1073
Adsorption	2.9	2.59	2.47	2.44
Desorption	2.83	2.5	2.4	2.35
Box-cluster (D_B)	1.93 ± 0.01	1.94 ± 0.01	1.955 ± 0.015	—
Perimeter–area Cluster (D_P)	1.09 ± 0.01	1.08 ± 0.01	1.06 ± 0.02	—

D_S is calculated by the Neimark adsorption/desorption method; D_S scaling interval $\in$ [2,3]. (ii) D_B and D_P are measured from TEM photographs; D_B scaling interval $\in$ [1.8, 2.1]; D_P scaling interval $\in$ [1,2].

confirming the textural conclusions pointed out before by the sorption analysis.

On the other hand, the fractal dimensions measured by TEM by the box-counting method (Table 4) cover the scale range from 5 to 200 nm, and therefore reflect mainly the aggregation process which gives rise to the gel rather than the fine molecular aspects of the pore surface. Fig. 6 depicts the kind of plot from which D_P and D_B values are calculated. In fact D_B and D_P are quite insensitive to thermal treatment after the gel was formed (Table 4). The D_B range value that is observed (i.e., between 1.8 and 2.1) indicates that the process of aggregation was not uniquely dominated by diffusion but that some reactive aggregation also took place. The insensitivity of D_P with temperature confirms, within the scale range mentioned, that aggregation phenomena are dominating the fractal nature of these gels. However, a slight decrease in D_P is manifested with annealing

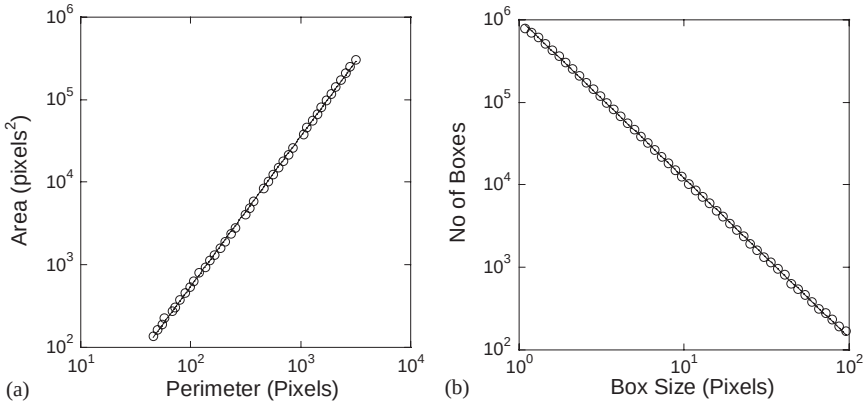

Fig. 6. Representative Benoit runs performed on a TiO_2–CeO_2-473 TEM micrograph. (a) Area-perimeter and (b) Box-counting fractal dimension determinations.

temperature, thus indicating that the surface smoothing mentioned before has some effect on this decrement.

4.4. Fractal and textural properties related to TiO_2–CeO_2 structure modelling

The particular fractal and textural properties attained by the collection of TiO_2–CeO_2 xerogels annealed at different temperatures can be related to the occurrence of three phenomena: (i) the possible replacement of some Ti^{4+} by Ce^{4+} ions inside the TiO_2 structure to form solid TiO_2–CeO_2 solutions, (ii) the crystalline phase change undertaken by TiO_2 when transforming from the anatase structure to the rutile form [40] as a consequence of thermal treatment at temperatures from 873 onwards, and (iii) the emergence of cerianite crystals on the surface of TiO_2 grains as the annealing temperature is increased.

Let us state some ideas regarding the possibility that these three processes can arise thus influencing the properties of annealed TiO_2–CeO_2 xerogel materials. First let us recollect that sol–gel materials can render a broad assortment of diverse nanostructures if compared to those attained by other procedures [41]. Colloidal sol–gel compounds, in particular, pure TiO_2 or mixed TiO_2–CeO_2 xerogels, present a great deal of electronic and geometric defects. During the gelation process, the precursor Ti alkoxide compound produces a large amount of alkoxy and hydroxy groups which, almost concurrently to their formation, condense to create the oxide precursory compound. Nevertheless, when the Ti colloid is being dried, ^-OH species can be located throughout the titania [42] and titania-ceria matrices while remaining stable towards thermal treatment up to 1073 K. This provokes an excess of positive charges in the material which are balanced by free electrons and oxygen vacancies; all these phenomena can deeply affect the structure and texture of the resultant titania-ceria products. In general, colloids constitute amorphous structures; nevertheless, these substrates are sometimes composed of nanocrystalline structures (10–25 nm) dispersed in such a way that the final properties are more alike to those of a colloid than to conventional crystal arrangements. As the annealing temperature is increased TiO_2–CeO_2 xerogels undergo a dehydroxylation process, this phenomenon occurring in a series of steps and a maximum rate appears at 723 K [42]. Furthermore, TiO_2–CeO_2 sol–gel final products are a combination of two transition elements, the ultimate characteristics of such kind of mixed oxide sol–gel materials are not the summation of the properties of individual components but those of a hybrid material displaying innovative features.

The anatase crystalline structure includes interstitial channels in which doping Ce^{4+} coordinated species can gain access in order to substitute some Ti^{4+} moieties. When linear or branched $\equiv Ti–O^-$ chains are being formed in the sol state, Ce^{4+} can be inserted in between these chains by direct linking or substitution of one Ti^{4+} to finally obtain a $\equiv Ti–O–Ce–O–Ti\equiv$ xerogel arrangement. The whole TiO_2 network can be saturated with relatively small amounts (i.e., ppm) of Ce (this being a consequence of the relative large difference between the atomic radii of Ti^{+4} and Ce^{+4} ions), while the rest of this element can be found dispersed on the surface as CeO_2. A crystal simulation software program [43] has been used to try introducing a Ce atom into the anatase network by substitution of a Ti atom; Fig. 7 displays the structure of the solid solution simulated this way and, at least from the stereo chemical point of view, no problems were detected for this Ce inclusion in the anatase network. The possibility of the latter fact can be one major cause of the variety of surface fractal dimensions that were found in this work by N_2 sorption measurements on TiO_2–CeO_2 samples annealed at different temperatures.

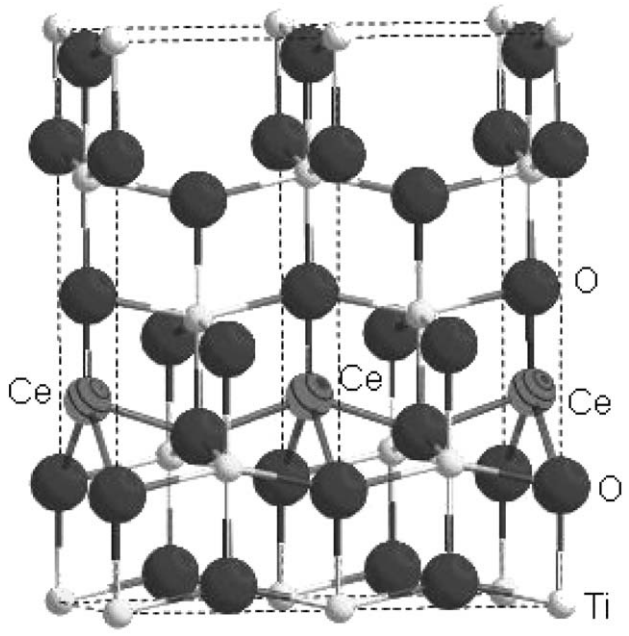

Fig. 7. Replacement of Ti^{4+} ions by doping Ce^{4+} species in the anatase network.

5. Conclusions

The textural properties of particle clusters, porous space and surface of TiO_2–CeO_2 substrates are the result of different physicochemical processes. Between annealing temperatures of 473–873 K, the pore structure of these materials correspond to inkbottle systems in which the cavity sizes are not very different from their delimiting throats. The pore-size distributions calculated from a NLDFT approach and assuming cylindrical voids confirm the previous idea, especially for samples treated at 673 and 873 K. Besides, the shapes of the PSDFs indicate the existence of a pore-blocking effect along a region of the DBC isotherm corresponding to the sample treated at 473 K, while this effect is slighter for samples annealed at 673 and 873 K. Additionally, the PSDFs of all materials suggest that the ABC isotherm is relatively free of cooperative mechanisms during the adsorbate uptake. The phase transition from anatase to rutile takes place above 873 K; the TiO_2–CeO_2 specimen treated at 1073 K contains a preponderant amount of rutile phase and has practically no pores. According to the values of fractal dimensions, the aggregation of sol precursor particles in the form of a fractal gel is dominated by both diffusion-controlled and reaction-controlled mechanisms. The TiO_2–CeO_2 xerogels adopt a surface fractal dimension value that depends on the rugosity of the final material after the annealing process at different temperatures; for samples subjected at low annealing temperatures the surface fractal dimension is larger than for materials treated at higher temperatures. It seems likely that cerium affects the crystallographic and sintering characteristics of TiO_2–CeO_2 compounds due to the progressive segregation of cerianite on the surface of TiO_2 globules as the temperature is raised and by substitution of Ti^{4+} by Ce^{4+} species within the TiO_2 anatase structure.

References

[1] N. Kholmanov, E. Barborini, S. Vinati, P. Piseri, A. Podestà, C. Ducati, C. Lenardi, P. Milani, Nanotechnology 14 (2003) 1168.
[2] X. Bokhimi, A. Morales, O. Novaro, T. López, E. Sánchez, R. Gómez, J. Mater. Res. 10 (1995) 2778.
[3] T. López, E. Sánchez, Mater. Lett. 25 (1995) 271.
[4] X. Bokhimi, A. Morales, O. Novaro, T. López, O. Chimal, M. Asomoza, R. Gómez, Chem. Mater. 9 (1997) 2616.
[5] T. López, R. Gómez, G. Pecchi, P. Reyes, O. Novaro, Mater. Lett. 40 (1999) 59.
[6] G. Rao, H.R. Sahu, Proc. Indian Acad. Sci. 113 (2001) 651.
[7] S. de Carolis, J.L. Pascual, L.G.M. Pettersson, J. Phys. Chem. B 103 (1999) 7627.
[8] J.E. Huheey, Inorganic Chemistry, Harper & Row, New York, 1975, p. 74.
[9] K. Tanabe, H. Hattori, T. Sumiyoshi, K. Tamaru, T. Condo, J. Catal. 53 (1978) 1.
[10] B.M. Reddy, A. Khan, Y. Yamada, T. Kobayashi, S. Loridant, J.C. Volta, J. Phys. Chem. B 107 (2003) 5162.
[11] T. López, J. Hernández-Ventura, R. Gómez, F. Tzompantzi, E. Sánchez, X. Bokhimi, A. García, J. Mol. Catal. A: Chem. 167 (2001) 101.
[12] M. Picquart, L. Escobar-Alarcón, E. Torres, T. López, E. Haro-Poniatowski, J. Mater. Sci. 37 (2002) 3241.
[13] A.V. Neimark, Ads. Sci. Technol. 7 (1991) 210.
[14] K. Falconer, Techniques in Fractal Geometry, Wiley, New York, 1997.
[15] A. Balankin, Eng. Fracture Mech. 57 (1997) 135.
[16] A. Balankin, A.D. Izotov, V.U. Novikov, Inorg. Mater. 35 (1999) 1047.
[17] E.P. Barrett, L.G. Joyner, P.P. Halenda, J. Am. Chem. Soc. 73 (1951) 373.
[18] R.W. Cranston, F.A. Inkley, Adv. Catal. 9 (1957) 143.
[19] M.L. Ojeda, J.M. Esparza, A. Campero, S. Cordero, I. Kornhauser, F. Rojas, Phys. Chem. Chem. Phys. 5 (2003) 1859.
[20] W.W. Lukens, P. Schmidt-Winkel, D. Zhao, J. Feng, G.D. Stucky, Langmuir 15 (1999) 5403.
[21] V. Mayagoitia, F. Rojas, I. Kornhauser, J. Chem. Soc. Faraday Trans. 1 (81) (1985) 2931.
[22] P.I. Ravikovitch, G.L. Haller, A.V. Neimark, Adv. Colloid Interface Sci. 76–77 (1998) 203.
[23] P.I. Ravikovitch, A.V. Neimark, J. Phys. Chem. B 105 (2001) 6817.
[24] M. Kruk, M. Jaroniec, Langmuir 13 (1997) 6267.
[25] J.M. Haynes, in: D.H. Everett (Senior Reporter), Specialist Periodical Reports, The Chemical Society, London, 1975, p. 1.
[26] P.I. Ravikovitch, A.V. Neimark, Langmuir 18 (2002) 1550.
[27] A.V. Neimark, P.I. Ravikovitch, J. Phys.: Condens. Matter 15 (2003) 347.
[28] J.M. Haynes, in: D.H. Everett, R.H. Ottewill (Eds.), Surface Area Determination, Butterworths, London, 1970, p. 97.
[29] B.B. Mandelbroot, The Fractal Geometry of Nature, Freeman, New York, 1983.
[30] BENOIT 1.2, http://www.trusoft-international.com
[31] K.S.W. Sing, D.H. Everett, R.A.W. Haul, L. Moscou, R. Pierotti, J. Rouquerol, T. Siemieniewska, Pure Appl. Chem. 57 (1985) 603.

[32] S.J. Gregg, K.S.W. Sing, Adsorption. Surface Area and Porosity, Academic Press, London, 1982.
[33] R.H. López, A.M. Vidales, G. Zgrablich, Langmuir 16 (2000) 6999.
[34] A.P. Karnaukhov, in: S. Modry (Ed.), Pore Structure and Properties of Materials, Vol. I, Academia, Prague, 1973, p. A-3.
[35] V. Mayagoitia, F. Rojas, I. Kornhauser, J. Chem. Soc. Faraday Trans. 1 (84) (1988) 785.
[36] D.H. Everett, J.M. Haynes, J. Colloid Interface Sci. 38 (1972) 125.
[37] D.H. Everett, in: E.A. Flood (Ed.), The Solid- Gas Interface, Vol. 2, Dekker, New York, 1967, p. 1055.
[38] R.A. Young, IUCr Monographs on Crystallography, No. 5, International Union of Crystallography, Oxford Science Publications, Oxford, 1993.
[39] F. Zhang, S.W. Chan, J.E. Spanier, E. Apak, Q. Jin, R.D. Robinson, I.P. Herman, Appl. Phys. Lett. 80 (2002) 127.
[40] J.T. Bastow, H.J. Withfield, Chem. Mater. 11 (1999) 3518.
[41] R. Scherer, G.W. Scherer, J. Non-Cryst. Solids 100 (1988) 77.
[42] T. López, P. Bosch, F. Tzompantzi, R. Gómez, J. Navarrete, E. López-Salinas, M.E. Llanos, Appl. Catal. A 197 (2000) 107.
[43] CrystaMaker Software, P.O. Box 183, Bicester, Oxfordshire, OX6 7BS, UK http://www.crystalmaker.co.uk